

Combining magnetic resonance imaging and ultrawideband radar: A new concept for multimodal biomedical imaging

F. Thiel,^{1,a)} M. Hein,² U. Schwarz,² J. Sachs,² and F. Seifert¹

¹Physikalisch-Technische Bundesanstalt, Braunschweig and Berlin, Germany

²Institut für Informationstechnik, Technische Universität Ilmenau, Germany

(Received 1 September 2008; accepted 15 December 2008; published online 9 January 2009)

Due to the recent advances in ultrawideband (UWB) radar technologies, there has been widespread interest in the medical applications of this technology. We propose the multimodal combination of magnetic resonance (MR) and UWB radar for improved functional diagnosis and imaging. A demonstrator was established to prove the feasibility of the simultaneous acquisition of physiological events by magnetic resonance imaging and UWB radar. Furthermore, first *in vivo* experiments have been carried out, utilizing this new approach. Correlating the reconstructed UWB signals with physiological signatures acquired by simultaneous MR measurements, representing respiratory and myocardial displacements, gave encouraging results which can be improved by optimization of the MR data acquisition technique or the use of UWB antenna arrays to localize the motion in a focused area. © 2009 American Institute of Physics. [DOI: 10.1063/1.3065095]

I. INTRODUCTION

Probing the human body with microwaves can be defined as seeing the internal structure of an object by exposing the object to low-power electromagnetic fields at frequencies in the range from 300 MHz to 300 GHz. If the exposition is done using a broadband signal, e.g., an appropriate pulse or a noise such as signal, rather than a single frequency, more information on dielectric composition and spatial and temporal arrangements can be acquired at a single shot.

A transmitter sensor (typically an antenna) can be used to illuminate the object with microwaves which propagate through the object and are detected by receiver antennas at the other side of the object. Another technique is to look for reflections, using either the transmitter itself or a separate device for detection (Fig. 1) (radar technique, radio detection, and ranging¹). The measured data can be processed by suitable reconstruction algorithms to provide information on the complex dielectric permittivity of the scattering object or on the motion of interfaces due to, e.g., human heartbeat and respiration.²

Noncontact detection and monitoring of human cardiopulmonary activity through bedding and clothing would be a valuable tool in sleep monitoring and home health care applications. Patients with conditions that can be perturbed or worsened by contact sensors include neonates, infants at risk of sudden infant death syndrome, and burn victims; a noncontact heart and respiration rate monitor could provide vital signs monitoring without affixed electrodes for these patients. Most alternatives to standard heart and respiration monitors need leads and contacts and often require accurate control or placement. This may be impossible or undesirable in many situations. In addition, a noncontact sensor could be used in situations where individuals need to move between

measurement stations without the restriction of electrodes, leads, or cuffs. A vital signs monitor that can sense contactlessly and through clothing would be ideal in these situations.³

The specific advantages of ultrawideband (UWB) radar sensors for medical applications are the high temporal and spatial resolutions due to the large bandwidth (up to 10 GHz), the deep penetration into objects (which is most pronounced at lower frequencies), the low integral power, and the compatibility with established narrow band systems.⁴ Due to the utilization of ultralow-power signals this technology permits noninvasive sensing without known risks, in contrast to catheter or x-ray techniques. Hence, it is particularly suitable for human medical applications, including mobile and permanent noncontact supervision of vital functions.⁵

Multimodal diagnostic approaches combine complementary information from different sources and with different sensitivities or resolution, e.g., to remove ambiguities from inverse problems. Hence, deriving correlated parameters from multimodal imaging is the primary motivation for the development of these techniques. Magnetic resonance imaging (MRI) with its wide range of applications is very well suited to be combined with other modalities and a variety of techniques, such as ultrasound (US),⁶ positron emission tomography (PET),⁷ single photon emission tomography,⁸ electroencephalography,⁹ electrocardiography (ECG),¹⁰ or optical tomography,¹¹ have already been used to this end. Some of these combinations are still in a rather experimental stage while others are routinely used in clinical practice.

An example for the latter is ECG triggering for cardiac MRI, a specifically challenging task due to heart beat and respiration related motions.^{12,13} Usually, MRI uses ECG information to acquire an image over multiple cardiac cycles by collecting segments of *k*-space at the same delay within the cycle. This requires breath hold as it is assumed that

^{a)}Electronic mail: florian.thiel@ptb.de.

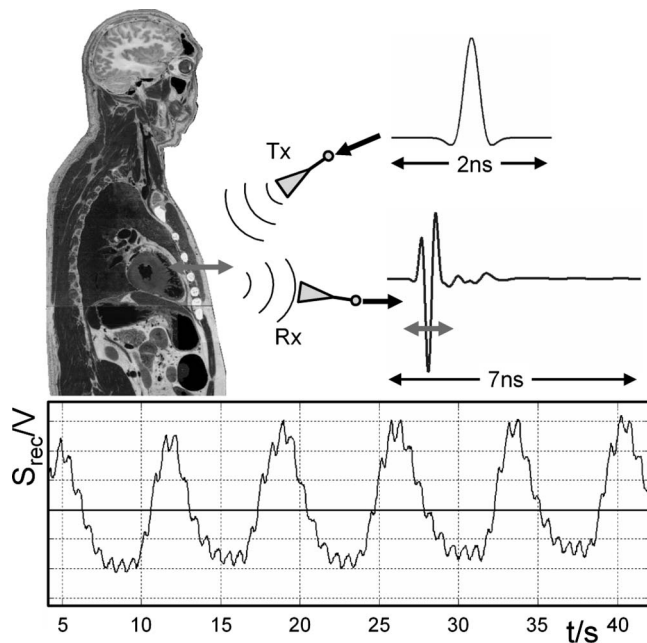


FIG. 1. Probing the human body with broadband electromagnetic pulses. Top: Transmitted pulse and received pulse (IRF of the scenario, IRF) which is modulated by the vital functions. Bottom: Reconstructed physiological signature S_{rec}^N , breathing with superimposed heartbeat, reconstructed from ultrawideband radar data. Anatomic slice taken from Ref. 17.

cardiac positions are reproducible over several ECG cycles. Unfortunately, in clinical situations many subjects are unable to hold their breath. High resolution MRI acquisition in the free-breathing state is of high clinical relevance, as hemodynamic parameters may differ between breath holding and free breathing. It has been shown that heart motion during respiration has a different pattern during inspiration and expiration. At high (≥ 3 T) and ultrahigh fields (≥ 7 T), ECG triggering is additionally hampered by the corruption of the ECG due to the magnetohydrodynamic effect.¹⁴

Our research aims at the synergetic technological development of UWB sounding combined with MRI, to explore its efficacy in such innovative fields of application as the imaging of coronary arteries, heart-beat monitoring, and accurate modeling of electromagnetic wave propagation through heterogeneous, malignant, and benign biological tissue, and fast and precise identification and localization of breast tumors.

II. METHODOLOGY

To evaluate the feasibility of a combination of MRI and UWB radar for improved functional diagnosis and imaging, a demonstrator has been implemented. This device allows the simultaneous detection of predefined motions of layered dielectric phantoms with MRI and UWB radar inside a 3 T MR scanner. To this end, a movable MR-compatible phantom comprising a layered structure of dielectric materials was to be designed and built, whose reflection properties mimic those of the human thorax. The phantom development took advantage of the results of a numerical model simulating the reflected signals (impulse responses) of multilayered, lossy dielectric structures. Algorithms and strategies for the

extraction of motion from raw UWB data had to be developed and tested under harsh MR conditions on phantoms, and *in vivo* on known physiological signatures.

A. Ultrawideband radar

The goal of UWB radar is to obtain the impulse response function (IRF) of a certain object under test (Fig. 1). The quality of a measured IRF is mainly determined by the ability to separate closely located peaks and to avoid the masking of smaller peaks due to noise or saturation effects caused by larger signals. The first problem is a question of available frequency bandwidth while the second depends on the dynamic range of the receiver and on transmitted power. The classical UWB approach is based on impulse excitation (Fig. 1), which implies that the whole transmission chain is subjected to high peak power. Mainly analog circuits tend to overload or saturate in such cases, and system performance degrades. In order to stress the electronics evenly, it is preferable to use continuous wideband signals. Typical examples of such signals are swept or stepped sine waves, random noise,¹⁵ or pseudonoise sequences. However, this kind of target stimulation will not provide the IRF directly. It rather requires an appropriate impulse compression technique (i.e., Fourier transform, correlation, or matched filtering), which is often the challenge for the different system concepts. Also, after impulse compression, the flat spectral energy distribution of the signals is lost. Thus, the best one can do is to carry out impulse compression in the digital domain. The digital dynamic range is only limited by the utilized data format which can usually be selected freely. A UWB concept dealing with continuous wave excitation, a largely reduced analog circuit part, and a minimum of components was first introduced in 1999.¹⁶ It provides *M*-sequence signals (see Sec. II B) to stimulate the test objects, which optimize the crest factor and therefore solve the overload and saturation problem. This original approach forms the basis for different extensions and improvements.

In Sec. II B, the basic structure of such an ultrawideband radar module is described.

B. The ultrawideband *M*-sequence base band module

The basic idea of an *M*-sequence (also called maximum length binary sequence) device initially intended for base band operations at, e.g., 0–5 GHz is known from a couple of former publications (see Refs. 18 and 19). A broader introduction in the theory of pseudorandom codes and their application is given in, e.g., Ref. 20. Figure 2 presents the basic structure of a wideband *M*-sequence device. The *M*-sequence—the stimulus signal for the object to be investigated—is generated by a digital shift register which is addressed by a stable rf clock with frequency f_c . The capturing of the measurement signal is accomplished by using a subsampling approach. This drastically reduces the hardware requirements since only the Track&Hold (T&H) circuit must be designed for rf purposes. One of the most important features of the *M*-sequence approach is that the actual sampling

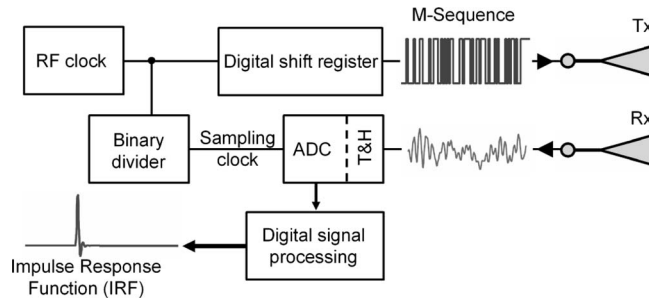


FIG. 2. Basic structure of the M -sequence (maximum length binary sequence) measurement head in block schematics (Refs. 18 and 19). T_x , R_x : transmit and receive antenna. T&H: Track and hold circuit.

rate f_s can be derived in a simple and stable way (i.e., by a binary divider) from the rf master clock such that $f_c = 2^n f_s$ (see Fig. 2 and Ref. 19 for details).

Time-domain measurements use correlation processing in order to gain the wanted IRF of the material under test. In that case, unwanted external narrow band perturbations will be spread over time, since they are not correlated with the test signal. In this way, they cause the same effect as white noise, which is often less critical than a corruption of the whole waveform in time domain, in the case of a classical time-domain reflectometry analysis, or the strong perturbation of individual frequency bands, in the case of network analysis.

III. COMPATIBILITY CONSIDERATIONS

Compatibility is the most challenging issue when combining MRI with other modalities. MR frequencies cover the range of $f \approx 30\text{--}300$ MHz, depending on the static magnetic flux density B_0 ($f/B_0 = 42.5$ MHz/T for protons). Sources of interference are the high B_0 values (1.5–7 T), the fast varying magnetic fields (up to 50 T/s) from switching magnetic gradient fields, and the high rf pulse power (approximately kilowatts) of a MR scanner. Magnetic impurities, vibrations, and the rf emission of complementary equipment may also result in severe image artifacts. Furthermore, patient safety may be impaired when combining MR with other techniques. In a first step, the available UWB hardware was checked with respect to compatibility with MR. These tests comprised inspection of the UWB device and antennas for ferromagnetic materials, checking the mutual coupling between the MR scanner's rf system and the UWB devices, testing for necessary acoustic damping of the UWB hardware to avoid image artifacts due to magnetic gradient switching, and checking for synchronous operation of the UWB radar with the MR scanner electronics.

The UWB device used in this article, generates signals covering the frequency band from dc to 5 GHz. The UWB antennas applied reduce this frequency range down to the range from 1 to 5 GHz due to there high pass properties.

The signal-to-noise ratio of a MR scan is not affected by the UWB signals, since the receiver bandwidth of 10–100 kHz is very low compared to the gigahertz bandwidth of the UWB system, moreover the antennas attenuate the transmitted UWB signal at 125 MHz, the Larmor frequency of protons at 3 T, by more than 100 dB. Comparing MR images

taken from a MR head phantom with and without UWB exposure, within measuring uncertainty, no additional noise could be observed. So, according to expectation, the MRI system was not affected by the UWB signals, as these appear as a low-power noise source to the MR system.

The results of these pilot investigations were incorporated in an improved design of MR-compatible versions of the UWB radar electronics unit (MEODAT GmbH, Ilmenau, Germany). Further criteria for safe UWB/MR equipment were also specified and included in the new design to fulfill the specific demands of the medical device directive.²¹

The design of UWB antennas usually does not take into account adaptation and compatibility issues for MRI. When a stationary conductor of area A_B encounters a spatially homogeneous, time-dependent magnetic field dB/dt , e.g., a switched magnetic-field gradient (~ 45 mT/m in 200 μ s) or a rf pulse, eddy currents are created. Eddy currents will be generated wherever a conducting object experiences a change in the intensity or direction of the magnetic field at any point within it. From Faraday's law the integral current $i(t)$ in a conductor of cross section A_i and length l can be deduced:

$$i(t) = - \frac{d}{dt} \frac{A_B A_i(\omega) \sigma}{l}, \quad (1)$$

where σ denotes the conductivity of the conductor. Note that the cross section A_i is frequency dependent due to the penetration depth:

$$d = \sqrt{\frac{2}{\sigma \mu \omega}}. \quad (2)$$

If the thickness of the plate is much larger than the penetration depth d the area $A_i \propto d$.

Since the current $i(t)$ from [Eq. (1)] flows within the static magnetic field of the MR scanner, the electrons in the conductor experience a *Lorentz force* perpendicular to their motion.

Experimentally, we observed sizable physical vibrations of unadapted antennas due to Lorentz forces on the eddy currents induced by the periodically switched field gradients of the MR scanner.

For MR-compatible antenna design the following criteria are therefore crucial: (i) The antenna should not contain ferromagnetic parts of any kind. (ii) Eddy currents due to the fast-switching magnetic-field gradients must be minimized in order to eliminate mechanical oscillations of the antennas. (iii) The voltages induced at the antenna feed point by the magnetic-field gradients and the rf signal have the potential to damage the radar device input stage. The first point can be fulfilled by building the antennas from copper or other diamagnetic metals. The second and third points can be achieved mutually by reducing the area A_B penetrated by the B field and increasing the resistance of the eddy currents path. This can be done most effectively by reducing the area A_i seen by the eddy currents (minimum thickness of the metal layer) and increasing the path length l , e.g., by meandering slitting of the remaining areas. The induced voltage due to the high rf pulse power can further be reduced by shielding of the antennas.

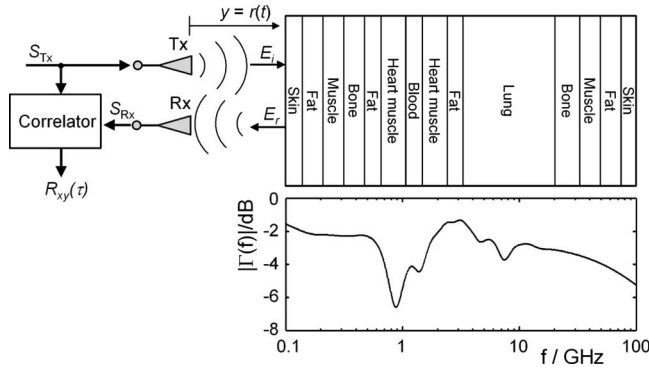


FIG. 3. UWB radar probing a multilayered dielectric structure (bistatic setup). S_{Tx}/S_{Rx} : transmitted/received signal; T_x/R_x : transmit/receive antenna; E_i/E_r : incident/reflected electrical field component; $R_{xy}(\tau)$: correlation result from UWB device; $\Gamma(f)$: reflection coefficient. Top right: Layered arrangement to mimic the reflective properties of the human thorax (not to scale). Bottom right: Calculated magnitude of the reflection response $\Gamma(f)$ which is equivalent to the frequency response function of the object.

While some of these requirements can be easily implemented in a modified antenna design, the geometrical form and arrangement of conducting and insulating regions require careful consideration, as the radiation properties of the antennas such as radiation pattern or frequency dispersion of the radiated pulses are entirely determined by the excited rf currents.

IV. MODELING

Figure 1 and, in a more abstracted way, (Fig. 3) depict the setup commonly used to probe the human body with a UWB device. The body can be assumed to form a multilayered dielectric structure with a characteristic reflection coefficient $\Gamma(f)$. The UWB signal, which can be a pulse or a pseudonoise sequence⁴ of up to 10 GHz bandwidth, is transmitted utilizing appropriate pulse-radiating antennas T_x (e.g., horn or tapered slot antennas). The reflected signal is detected by R_x and calculating the correlation between received signal S_{R_x} and transmitted signal pulse S_{T_x} is usually the first step in further signal processing.

Accurate numerical techniques to predict the propagation of UWB signals in biological tissue are of great interest to researchers as an aid to developing signal processing algorithms. Thus, we implemented a layered tissuelike model to address problems such as: (i) How many dielectric layers are needed for a phantom to achieve a reflection coefficient closely approximating the reflective properties of the human thorax?, or (ii) how do propagation time and power losses evolve while the electromagnetic waves traverse each layer? Furthermore, the influence of physiological processes such as breathing and cardiac motion on the reflection coefficient can be studied. We constructed our model from 14 planar isotropic layers whose arrangement as well as individual thicknesses approximated a transthoracic slice from the visual human data set¹⁷ (Fig. 1). The spectral response of a dielectric medium is suitably described in terms of multiple Cole–Cole dispersion [Eq. (3)] which, with a choice of pa-

rameters appropriate to each constituent, can be used to predict the dielectric behavior over the desired frequency range²²

$$\varepsilon(\omega) = \varepsilon_\infty + \sum_{m=1}^4 \frac{\Delta\varepsilon_m}{1 + (j\omega\tau_m)^{(1-\alpha_m)}} + \frac{\sigma_i}{j\omega\varepsilon_0}, \quad (3)$$

where up to four Cole–Cole dispersions in the frequency range $f=10$ Hz–100 GHz are considered. $\omega=2\pi f$; ε_∞ : permittivity for $\omega \rightarrow \infty$; ε_0 : permittivity of free space; $\Delta\varepsilon_m$: change in ε in the individual dispersion region; τ_m : mean relaxation time constant of the individual dispersion region; α_m : distribution parameter describing the broadening of the dispersion, i.e., the broadening of the distribution of time constants around τ_m ; σ_i : ionic conductivity in the static case. In the case of a stationary ε , $\Delta\varepsilon_m=0$ outside the dispersion region, the imaginary part of $\varepsilon=\varepsilon'-j\varepsilon''$ is exclusively determined by the conductivity $\sigma=\varepsilon''\varepsilon_0\omega$.

This information is also incorporated in the model. For such a layered arrangement (Fig. 1), the reflection response, which is equivalent to the transfer function of the object, can be recursively calculated using Ref. 23,

$$\Gamma_i(\omega) = \frac{\rho_i + \Gamma_{i+1}e^{-2jk_i l_i}}{1 + \rho_i \Gamma_{i+1}e^{-2jk_i l_i}}, \quad (4)$$

with $i=M, M-1, \dots, 1$, where M is the number of layers. ρ_i is the specific reflection coefficient of each interface: $\rho_i = (1 - \sqrt{\varepsilon_i/\varepsilon_{i-1}})/(1 + \sqrt{\varepsilon_i/\varepsilon_{i-1}})$; Γ_i the reflection response at the i th interface, initialized by $\Gamma_{M+1}=\rho_{M+1}$. With l_i and $k_i(\varepsilon', \varepsilon'')$ we denote the thickness and the propagation parameter, respectively, of the i th layer. ε' denotes the real part and ε'' the imaginary part of complex permittivity ε from Eq. (3).

Given that, the received signal S_{R_x} in the frequency domain becomes

$$S_{R_x} = S_{T_x} H_{T_x} H_{R_x} \Gamma \exp(-2j\omega r/c_0)(2r)^{-1}, \quad (5)$$

with H_{T_x} are H_{R_x} are the transfer function of the transmitting and receiving antennas, respectively. The factor $(2r)^{-1}$ is introduced to account for the path dependent damping of a spherical electromagnetic wave reflected on a plane, extended surface in the far field. The reflection on a point target is again the source of a spherical wave which results in r^{-2} . The exponential function accounts for the time delay between transmitted and received signal due to the propagation in free space.

Finally, the output of the correlator in Fig. 3 becomes

$$R_{XY}(\tau) = \int S_{T_x}(t + \tau) \cdot S_{R_x}(t) dt = S_{T_x}(\tau) \circ S_{R_x}(-\tau), \quad (6)$$

where \circ represents the convolution operator.

As a first result of our modeling, we calculated the evolution of propagation time τ and power losses while the electromagnetic waves traverse each layer at different frequencies (Fig. 4).

The propagation time τ after the i th layer is defined as follows:

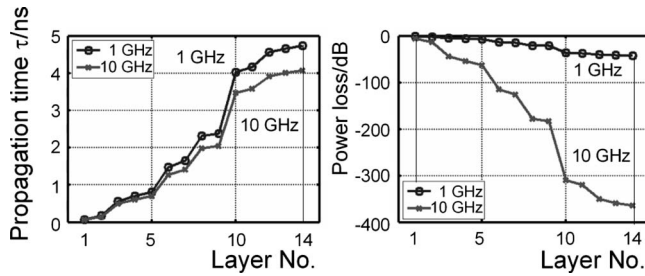


FIG. 4. Propagation of a plane electromagnetic wave (1 and 10 GHz) through the 14-layered dielectric model. Left: Evolution of propagation time τ at each layer. Right: Evolution of power losses at each layer.

$$\tau = \frac{1}{c_0} \sum_{i=1}^{14} l_i \sqrt{\epsilon'_i}. \quad (7)$$

The power per unit area flowing past the point y in the forward y -direction will be

$$P(y) = P(0)e^{-2\alpha y}, \quad (8)$$

where α denotes the attenuation constant:

$$\alpha_i = \text{Re}\{\omega \sqrt{\mu_i [\epsilon'_i(\omega) - j\epsilon''_i(\omega)]}\}. \quad (9)$$

Hence, the power loss after the n th layer become

$$A_n/dB = -20 \log_{10}(e) \sum_{i=1}^{n=14} \alpha_i \Delta y_i. \quad (10)$$

These data, together with the calculated frequency dependence of Γ , provide valuable information for application dependent radar sensor design (Fig. 4).

These data, together with the calculated frequency dependence of Γ (see Fig. 3), provide valuable information for application dependent radar sensor design.²⁴ With the aim to monitor myocardial function at its origin, the electromagnetic wave can be expected to reach the heart muscle at a depth of around 4 cm (layers 6–8, $1.5 \text{ ns} < \tau < 2.5 \text{ ns}$). Application of a 1 GHz signal implies penetration through the whole body, with a signal attenuation of about 50 dB at the back. With a good receiver and appropriate signal processing techniques myocardial deformation should be detectable even with frequencies of up to 10 GHz.

V. MRI/UWB RADAR PHANTOMS

Phantoms which closely mimic the physical properties of various human tissues have always been indispensable for the development and testing of medical imaging modalities, such as US, MRI, or computed tomography. To evaluate a combined MR-UWB technique, motion-controlled MR-compatible tissue phantoms are needed, mimicking both dielectric and NMR properties of biological tissue in the frequency range covered by the UWB technology. The *in vitro* dielectric properties of biological tissue are well known in a broad frequency range and can be used as an initial point for phantom development.²² In the desired frequency range, the highest values of ϵ' and ϵ'' (i.e., the electrical conductivity $\sigma = \epsilon'' \epsilon_0 \omega$) are very similar to those of aqueous solutions or emulsions of nondispersive molecules. The lowest dielectric tissue values are defined by fatty tissue. Therefore, we cre-

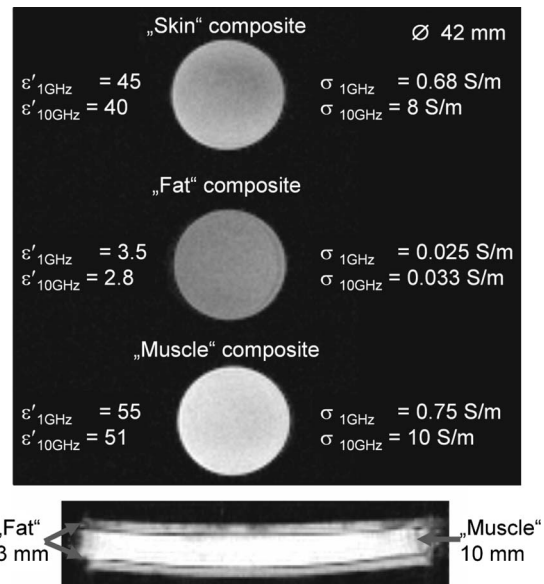


FIG. 5. Top: MR images of coronal slices of three tissue-mimicking composite samples ($\varnothing 42 \text{ mm}$) and their corresponding values of ϵ' and σ measured at 1 and 10 GHz. Bottom: Axial slice of a muscle-equivalent layered phantom ($\varnothing 150 \text{ mm}$) embedded in two fat-equivalent layers of 3 mm thickness (propane-1,2,3-triol doped silicon gel).

ated oil-in-water emulsions to mimic this behavior. These mixtures were stabilized in agarose gel (type II-B, Sigma-Aldrich), which retains enough elasticity for dynamic phantoms. The conductivity was adjusted by adding NaCl. We built planar, circularly shaped (diameter of 150 mm) slices to form multilayer dielectric phantoms (see Fig. 5, lower part). Low-permittivity materials such as fat were formed from a silicone gel (Sylgard A&B). To account for the finite conductivity of adipose tissue, the silicone gel was doped with glycerol (propane-1,2,3-triol) which can also be used to adjust the dispersive behavior of the aqueous mixtures and the silicone gel.

We measured the dielectric properties of the samples using a calibrated coaxial probe in conjunction with a network analyzer (Fig. 6). The MR compatibility and MR properties of the phantom materials were investigated by measurements with PTB's 3 T MR scanner (Bruker MEDSPEC 30/100) (Fig. 5). We found that the composition of the phantoms could indeed be adjusted to mimic the dielectric properties of all major organic tissue in the desired frequency range of 1–10 GHz within their biological variability of 15%–20%. Moreover, the mixtures are homogeneous and MR compatible. Since higher $|\epsilon|$ is in accordance with higher water content, and hence higher hydrogen content, the MR image intensity scales with $|\epsilon|$ because of the non-negligible imaginary part ϵ'' (Fig. 5).

As a further result of our modeling, we found that in the desired frequency range of 1–10 GHz, the reflective properties of the thorax are dominated by the first three layers (skin, fat, and muscle) (see Fig. 7). This result was used as a reference for the number of the planar, circularly shaped slices used for the construction of the multilayer dielectric phantoms.

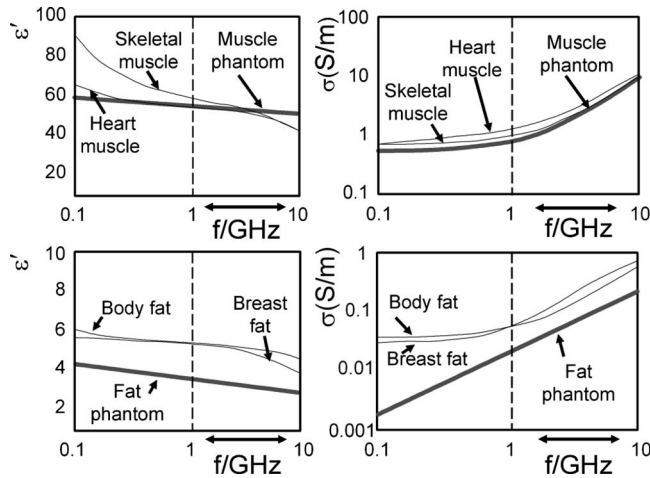


FIG. 6. Comparison of the measured values (bold gray line) of ϵ' and σ between 0.1 and 10 GHz with the corresponding values given by the literature (thin line) for two selected phantom materials (muscle and fat). The frequency range relevant for UWB radar (1–10 GHz) is indicated by the arrow and vertical dashed lines.

VI. MOTION RECONSTRUCTION ALGORITHM

To extract displacements of interfaces built from various biological tissues or multilayered phantoms, a number of algorithms were developed and tested. These algorithms are crucial to identify relevant signals in static and dynamic clutter, as well as to decompose significant physiological signatures from the multiple superimposed impulse responses generated by the object under test. Our algorithms are based on an analysis of eigenvalues, extracted from the covariance matrix \mathbf{Q} calculated from the cross-correlation data $\mathbf{R}_{xy}(\tau)$ of the transmitted and received signals. $\mathbf{R}_{xy}(\tau)$ is provided by the UWB controller where each of the N rows is an observation containing M samples, and each of the M columns represent a time shift $\Delta\tau$. If we define the rows of \mathbf{R}_{xy} to correspond to all measurements of a particular type and each column to a set of measurements from one particular trial, the covariance matrix becomes $\mathbf{Q} = 1/(N-1) \mathbf{R}_{xy} \mathbf{R}_{xy}^T$. \mathbf{Q} captures the correlation between all pairs of measurements. The covariance measures the degree of the linear relationship between two variables, where a large (small) value indicates high (low) redundancy. The main diagonal elements $\lambda_{\mathbf{Q}} = \{\lambda_{\mathbf{Q},11}, \dots, \lambda_{\mathbf{Q},MM}\}$ of \mathbf{Q} are the variance of particular measurement types and the off-diagonal terms are the covariance between measurement types. In the diagonal terms the interesting dynamic is reflected. Given that, we ignore redundancy information by setting the off-diagonal terms to zero, which results in a diagonal matrix \mathbf{D} :

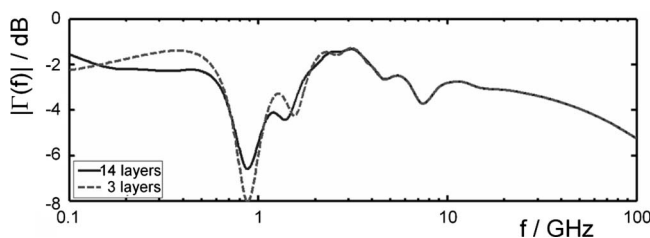


FIG. 7. Comparison of the reflection coefficient $\Gamma(f)$ for a 14-layered (bold line) and a 3-layered (dashed bold line) arrangement.

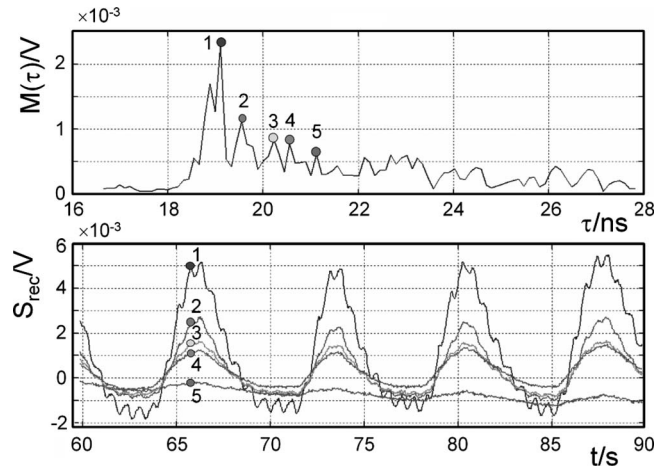


FIG. 8. Measured physiological signatures using the proposed algorithm [Eqs. (7) and (8)]. Upper graph: $M(\tau)$. Lower graph: Time courses S_{rec}^N corresponding to the labeled local maxima of $M(\tau)$.

$$\mathbf{D} = \text{diag}(\lambda_{\mathbf{Q}}). \quad (11)$$

Therefore the eigenvalues of the diagonal matrix \mathbf{D} for each time shift τ are contained by $\lambda_{\mathbf{Q}}$, those elements are an estimate of the momentary signal variance. Each eigenvalue corresponds to a certain time shift τ .

$$M(\tau) = \lambda_{\mathbf{Q}}(\tau). \quad (12)$$

If the influence of the antennas is extracted from the received signal by using deconvolution techniques, significant values in $M(\tau)$ directly correspond to relevant interfaces (large Γ and/or near the surface), which are displaced by physiological events (Fig. 8), e.g., the body surface or internal transitions from fat to muscle.

A physiological process, e.g., respiration and/or cardiac motion, generally displaces several interfaces in parallel, which give similar signals. Restricting the signal examination to the one indicated by the significant values defines a less-dimensional subspace of \mathbf{R}_{xy} .

The tissue layer arrangement of an individual morphology (phantoms or transthoracic) can readily be deduced from MR images. Combining this knowledge with the aforementioned layered model, the propagation time required by an electromagnetic wave to reach a specific layer or interface can be estimated. Thus, the time course corresponding to a selected interface can approximately be found in $M(\tau)$.

To affirm the validity of this algorithm it was tested on the described phantoms which were moved in a controlled way with high spatial precision (see Fig. 9: the setup is described in more detail later). Since the distances between the antennas and the multilayered phantoms are known as well as the thickness of the layers, the time courses corresponding to each interface are precisely defined.

For testing, we intentionally chose aggravated experimental conditions: (i) The distance between antennas and the phantom was four times larger than in the intended medical application; (ii) the radar cross sections of the phantoms were much smaller than those of the human thorax; and (iii) the lowest possible dielectric contrast was chosen, i.e., a fat-equivalent phantom.

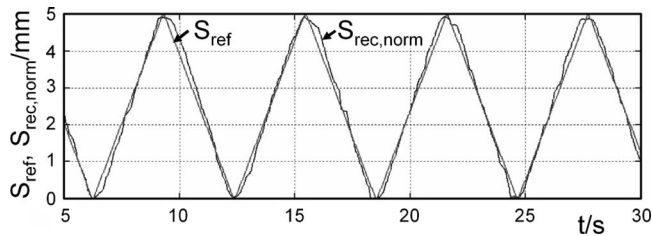


FIG. 9. Comparison of a triangular reference profile S_{ref} (gray line) with the normalized signal reconstructed from raw UWB data $S_{rec, norm} = [S_{rec}/S_{rec, max}]S_{ref, max}$ (black line). Maximal displacement $S_{ref, max} = 5$ mm, $f = 0.16$ Hz. Triangular reference profile. Distance to the antennas: 0.4 m.

We utilized an M -sequence UWB radar system⁴ (up to 5 GHz) transmitting a periodic, pseudorandom waveform (maximum length binary sequence) and tapered slot UWB antennas. Figure 9 depicts the comparison between the sawtoothlike reference profile which exhibits an amplitude of 5 mm at 0.16 Hz, and the time course of the displacement reconstructed from the raw UWB data.

From this result and further calculations it can be assumed that the resolvable motion amplitude lies well below 1 mm. The deviation from the reference can be explained by the compressibility and deflection of the leverage of 3 m length (Fig. 11) and by friction-induced sporadic discontinuities in the motion.

Furthermore, the algorithm was tested with stand-alone UWB measurements on a volunteer outside of the MR scanner mimicking the envisaged biomedical applications. These tests, particularly aiming to reproduce a breathing paradigm and the superimposed cardiac contraction, exhibit good correspondence between calculated time courses and physiological reality (Fig. 10). The test proved the ability of the algorithm to detect movements in the submillimeter range even for harsh experimental conditions and is therefore well suited for the envisaged application.

VII. COMBINED MR/UWB IMAGING

The demonstrator allows the computer controlled motion of our thorax phantoms inside the MR scanner's head coil (operated at 125.3 MHz) in the center of the scanner (Fig.

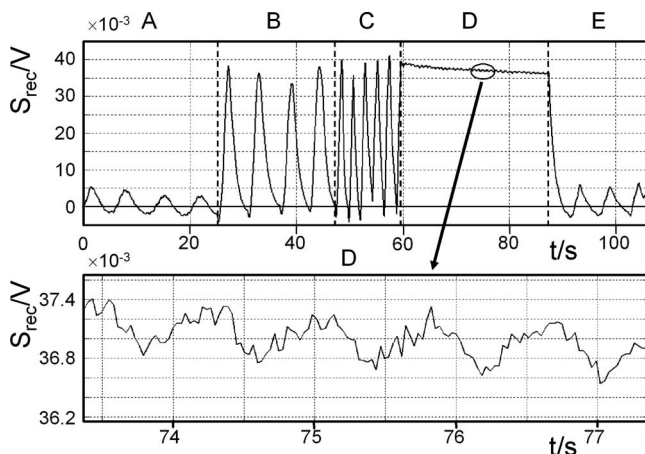


FIG. 10. Upper trace: Breathing paradigm: (a) normal breathing, (b) deeper breathing, (c) increased frequency, (d) breath hold, (e) normal breathing. Lower trace: Enlarged detail of segment (d) (breath hold).

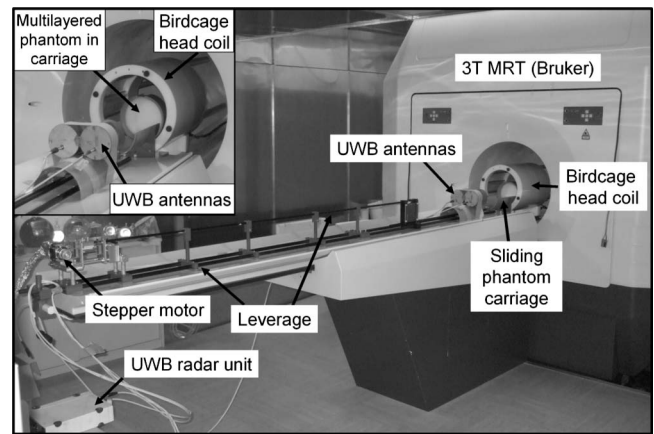


FIG. 11. Demonstrator setup inside the MR scanner. The inset shows an enlarged view of the phantom/antenna/head coil arrangement.

11). The motion is driven by a stepper motor over a long leverage (3 m). The nominal spatial resolution was $5.3 \mu\text{m}$ per step. The leverage connecting the motor with the sledge was built of carbon-fiber reinforced plastic to minimize compressibility and deflection. As can be seen in Fig. 9, there are deviations between reference profile and measurement which can be explained by the nonideality of the leverage and by friction-induced sporadic discontinuities in the motion. These uncertainties remain well below 1 mm, however, and are perfectly acceptable. The motional profile of the sandwich structure was shaped to approximate a respiratory-induced motion of the thorax, superimposed by cardiac oscillations. This is illustrated in Fig. 12. We utilized the aforementioned M -sequence UWB radar system⁴ and prototypes of MR-compatible tapered slot UWB antennas to detect the motion of the phantom inside the MR scanner.

The UWB antennas were placed perpendicularly to the sandwich structure at a distance of 0.4 m. For MR imaging, a flow-compensated gradient echo CINE sequence (time resolution: 50 ms) was used to reduce artifacts generated by the phantom motion. For synchronization, this sequence was triggered by the stepper motor controller. Sporadic image artifacts caused by higher order movements (acceleration) did not hinder the analysis of the MR data which was simply carried out by manual determination of phantom edges in the

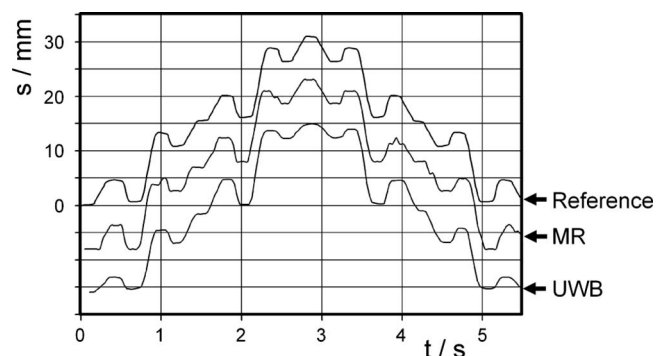


FIG. 12. Comparison of one period of the reference profile with the data obtained simultaneously by MRI and UWB radar measurements. For better clarity, the profiles obtained from MR and UWB radar measurements are offset by the initial values given in the chart.

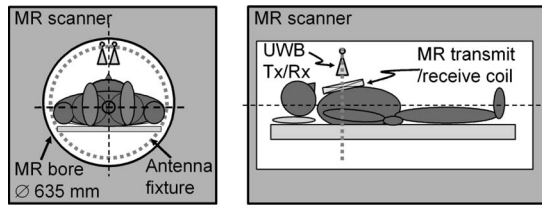


FIG. 13. Setup for simultaneous acquisition of physiological signatures with UWB radar and MRI.

128 time frames. Comparing the three independently measured data sets for the position of the phantom in Fig. 12, we find good agreement between the reference profile from the stepper motor controller, the edge positions determined by MRI, and the UWB measurements. Furthermore, the spatial resolution of the UWB radar is similar to that of MRI (~ 1 mm). The correlation between the time sequences derived from UWB radar and MRI exceeds 99.3%.

VIII. FIRST *IN VIVO* EXPERIMENTS

In the following, the setup for the simultaneous monitoring of respiratory and cardiac motion is described. A volunteer was positioned in supine position inside the MR scanner and was breathing spontaneously (Fig. 13). The MR-compatible tapered slot UWB antennas (T_x/R_x) are positioned about 100 mm above the sternum. A transmit/receive MR surface coil (220×150 mm²) operating at 125.32 MHz is centered underneath the antennas upon the sternum between the papillae mammae.

A photograph of the MR transmit/receive coil on a body water phantom is depicted in Fig. 14.

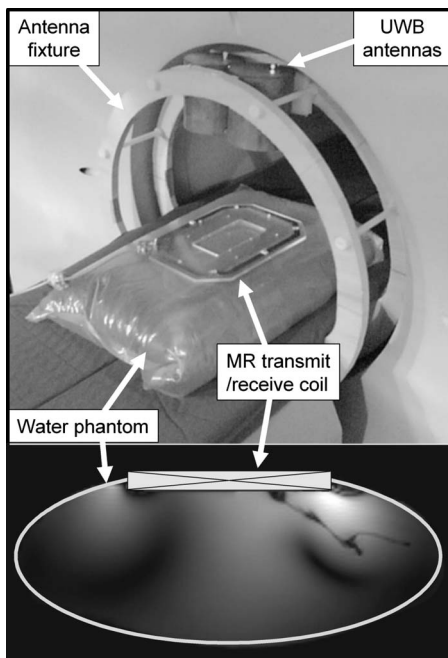


FIG. 14. Top: Transmit/receive MR surface coil (220×150 mm²) on top of a water body phantom, together with the UWB measurement setup located at the entry to the bore of the MR scanner. For the measurements the arrangement is placed inside the bore. Bottom: Sensitivity profile $\psi(x, y)$ of the MR transmit/receive coil in an axial slice of the phantom (not to scale). The image contrast scales with sensitivity $\psi(x, y)$.

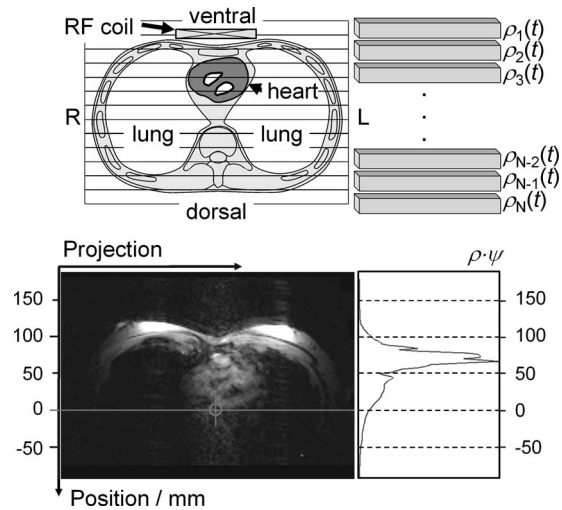


FIG. 15. Upper right: Fragmentation of the axial slice in columns of $2 \times 5 \times 512$ mm³, giving the integral signal intensity for the projection profile (lower right). Upper left: Anatomical sketch for orientation. View from the subject's feet toward the head. Lower left: Axial *in vivo* MR image (breath hold). The circled cross defines the center of the MR bore. Lower right: Projection profile (acquired within 50 ms) of one arbitrary state within the cardiac and respiratory cycle of the freely breathing subject.

The aperture of the coil gives enough space for the UWB signal. The reflection caused by the transparent support plastic material of the coil is negligible due to its low dielectric contrast. Reflection signals from the printed circuit board tracks arrive earlier than the body's reflection, and can be separated by our algorithm. The MR transmit/receive coil exhibits a characteristic overall sensitivity profile $\psi(x, y, z)$ (magnitude). For one selected axial slice $\psi(x, y)$ is depicted in Fig. 14 taken from a MR body water phantom.

It has to be mentioned, however, that this profile likely will be different from the actual sensitivity profile in a human torso at 3 T due to finite wavelength effects. The difference between a homogeneous water phantom and a human body will be even more pronounced at higher fields such as at 7 T. Nevertheless, the measured sensitivity profile is not used for correction of the data.

To assure sufficient time resolution for an accurate monitoring of cardiac and respiratory motions, we used a one-dimensional imaging technique to speed up data acquisition. This technique produces projection profiles of the integral signal intensity (roughly proton density ρ times coil sensitivity ψ) along horizontal columns of $2 \times 5 \times 512$ mm³ in an axial slice chosen in an appropriate transversal plane through the heart (Fig. 15). This signal reflects the positions of the chest wall and the heart, as the MR signal intensity of the surrounding lung tissue is negligibly small. The resulting profiles are weighted with the sensitivity profile of the MR surface coil which causes the fading of the projection profiles toward the back of the subject (Fig. 15, lower right).

The lower left panel of Fig. 15 presents an axial MR image of the volunteer during a breath hold. A flow-compensated gradient echo MR sequence was used to reduce artifacts generated by cardiac motion and blood flow. The remaining image artifacts in Fig. 15, lower left are caused by higher order movements (acceleration) accompanying the

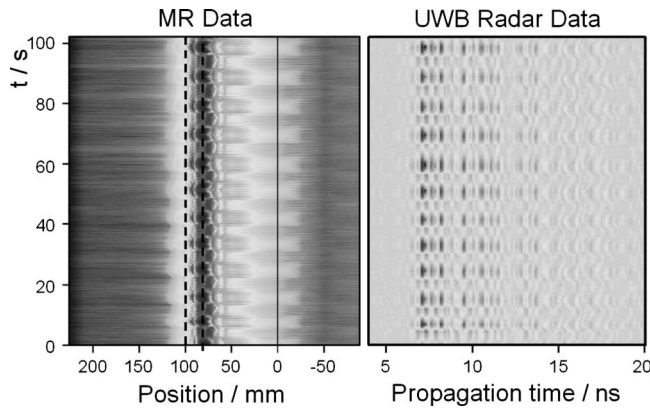


FIG. 16. Left: Temporal evolution of the projection profiles $\log(\rho\psi)$ measured by MRI. Right: Postprocessed UWB radar signal temporal evolution vs propagation time ($R_{xy}(\tau, t)$) showing corresponding periodic variations.

highly nonlinear motion of the heart during the breath hold. The corresponding one-dimensional (1D) projections of the same slice were taken every 50 ms allowing spontaneous breathing, as shown on the lower right of Fig. 15.

The temporal evolution of this 1D projection (profile) is affected by respiration and cardiac motion as shown in Fig. 16 on the left, where the logarithm of the signal intensity is displayed. Cyclic respiratory and cardiac activities are clearly visible along the time course.

UWB signals (e.g., pulses) propagate through the body tissue and are partly reflected at each interface, depending on the dielectric contrast of the materials. Starting from the front of the body and progressing toward the back, several interfaces are encountered. Thus the resulting reflected signal is a superposition of multiple reflections. In the simple case of well-separated interfaces, cross-correlation data $\mathbf{R}_{xy}(\tau)$ from the transmitted and received signals provide information on the propagation time τ necessary for the electromagnetic pulse to reach each interface. Interfaces with high dielectric contrast, e.g., fat/muscle or vice versa, as they occur at the body surface and the surface of the heart, dominate $\mathbf{R}_{xy}(\tau)$.

Since we are interested in the motion tracking of selected interfaces we observe the variation of $\mathbf{R}_{xy}(\tau)$ over time for each τ by a covariance analysis [Eqs. (11) and (12)]. The temporal evolution of postprocessed UWB radar signals versus propagation time is given in Fig. 16 (right), where the logarithm of the magnitude is displayed. Reflections from the scenario's background (static clutter) are subtracted from the measurement by extracting the mean value of the IRF.

Periodic respiratory activities clearly dominate the signal contrast. For illustrative purpose we took the maximum of $M(\tau)$ [Eq. (12)] which corresponds to the reflection signal from the body's surface and extracted the time course from the associated $\mathbf{R}_{xy}(\tau)$. We applied the same signal processing technique to the MR data set. Figure 17 displays the results of first *in vivo* experiments applying MRI and UWB radar simultaneously to a volunteer, applying this signal processing technique. Cyclic respiratory and cardiac activities are clearly visible along the time course, indicating the correct rendition of the recorded physiological events. Cross correlation of the two signals acquired by the complementary

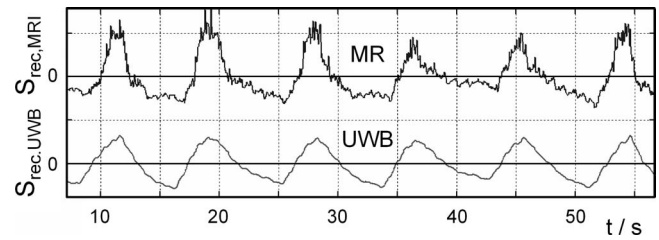


FIG. 17. Breathing with superimposed cardiac signal recorded simultaneously with MRI ($S_{\text{rec, MRI}} = S_{\text{rec, MRI}} / \max\{S_{\text{rec, MRI}}\}$) and UWB radar ($S_{\text{rec, UWB}} = S_{\text{rec, UWB}} / \max\{S_{\text{rec, UWB}}\}$) inside an MR scanner. Upper trace: Normalized 1D MRI signal of the horizontal spoke at $y=100$ mm in Fig. 15. Lower trace: Normalized corresponding surface UWB time series.

methods results in a correlation coefficient of 0.85 ($p < 10^{-10}$). The p -value denotes the probability that you would have found the current result if the correlation coefficient were in fact zero (null hypothesis). If this probability is lower than 5% ($p < 0.05$) the correlation coefficient is by convention considered statistically significant.

By the same physiological process, e.g., respiration and/or cardiac motion, a large number of interfaces are displaced in parallel. Searching for the corresponding signatures in the original data set using defined reference signals extracted from the aforementioned MR measurements, certainly gives ambiguous or even unphysical results, e.g., respiratory signals at propagation times much longer than those of the heart signal. Particularly higher noise levels favored the occurrence of such ambiguities.

A dimensional reduction in these data set by eliminating its redundant parts is crucial. Only in this way can uncorrelated, i.e., linearly independent signals, be analyzed. Our algorithm provides this reduction in dimension by an intuitive selection scheme. Another method to reduce dimension by creating uncorrelated signals formed from linear combinations of the source signals is carried out by principal component analysis (PCA).²⁵ In Fig. 18 we present the results given by PCA analysis. For illustrative purpose we used MRI-signatures from different body positions (surface $y = 100$ mm and a deeper position $y = 80$ mm) as reference signals to search correlatively in the PCA results calculated from the UWB data set. This was done for the purpose of investigating the motion signals at their origin, the respiratory signal from the surface and the myocardial signal from a deeper layer. Previously to the correlative search process we filtered the MRI and the UWB signals applying an infinite impulse response filter (respiratory signal: cutoff frequency of 0.4 Hz, cardiac signal: $0.7 \text{ Hz} < f < 5 \text{ Hz}$). Each minimum peak in the cardiac UWB signal represents a systolic cardiac contraction.

Cross correlation of the two respiratory signals acquired by the complementary methods results in a correlation coefficient of 0.85 ($p < 10^{-10}$) and the cross correlation of the two cardiac signals results in a correlation coefficient of 0.35 ($p < 10^{-10}$).

The remaining deviation of the signals from the two modalities can be explained by examination of the differences between the data acquisition techniques. While penetrating into the human body the UWB signal propagates in a three-dimensional manner and reflects the motion of a large area at

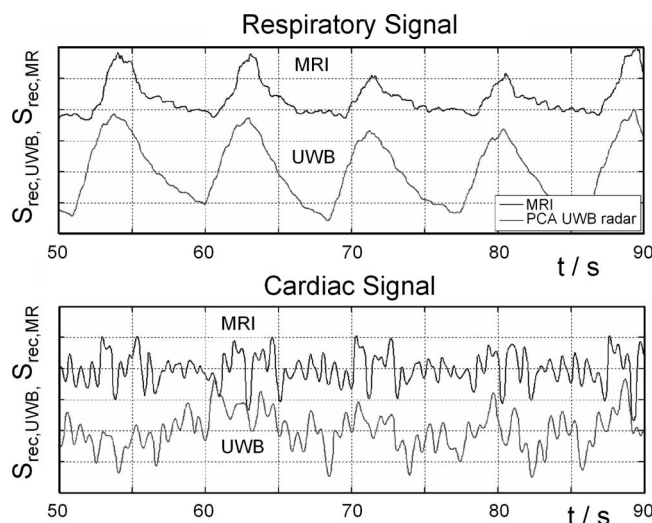


FIG. 18. Best correlatives of selected MRI components with PCA results from UWB radar data. $S_{\text{rec, MRI}} = S_{\text{rec, MRI}} / \max\{S_{\text{rec, MRI}}\}$, $S_{\text{rec, UWB}} = S_{\text{rec, UWB}} / \max\{S_{\text{rec, UWB}}\}$. Top: Respiratory signal (upper: 1D MRI-reference signal of the horizontal spoke at $y=100$ mm, lower: UWB radar). Bottom: Cardiac signal (upper: MR-reference 1D MRI-reference signal of the horizontal spoke at $y=80$ mm, lower: UWB radar). Each minimum peak in the cardiac UWB signal represents a systolic cardiac contraction.

a certain propagation time, e.g., the surface of the heart, which follows a cyclic highly nonlinear motion. The MR data acquisition technique we used, displays the variation of the integral proton density in a narrow volume, a column of $2 \times 5 \times 512$ mm³ in a selected axial slice. Considering this, the correlation results are very satisfactory and prove the ability of UWB radar to monitor physiological events directly at their origin inside the body. Optimization of the MR data acquisition technique or the use of UWB antenna arrays to localize the motion in a focused area, will improve the correlation result. Further improvements can be achieved if the measured sensitivity profile of the MR rf coil is considered for data correction.

IX. CONCLUSIONS

We proved the feasibility of a hybrid magnetic resonance and ultrawideband radar technique on phantoms. Our experiments were performed using a 3 T MR scanner but are also applicable to systems with higher field strength. These first results are very encouraging for the development of multimodal imaging techniques, combining complementary information from different sources, e.g., to remove the ambiguities from inverse problems, to improve the image quality of cardiac MRI, or to extend its range of applicability to less-cooperative patients.

ACKNOWLEDGMENTS

The authors are grateful to W. Hoffmann (PTB), F. Wojcik (PTB), M. Helbig, and R. Stephan from the Tech-

nische Universität Ilmenau for their technical and scientific support. We would also like to thank our medical partners I. Hilger and C. Geyer at the Institute for diagnostic and interventional radiology (FSU Jena). This work was supported by the German Research Foundation (DFG) in the U.K. oLoS priority program (No. SPP1202, project acronym ultra-MEDIS).

- ¹M. I. Skolnik, *Radar Handbook* (McGraw-Hill Education, Europe, 2008).
- ²H. J. Kim, K. H. Kim, Y. S. Hong, and J. J. Choi, *Rev. Sci. Instrum.* **78**, 104703 (2007).
- ³A. D. Droitcour, "Non-contact Measurement of Heart and Respiration Rates with a Single-Chip Microwave Doppler Radar," Ph.D. thesis, Stanford University, 2006.
- ⁴J. Sachs, P. Peyerl, S. Wöckel, M. Kmec, R. Herrmann, and R. Zetik, *Meas. Sci. Technol.* **18**, 1074 (2007).
- ⁵C. Leong, S.W. Sim, and C.K. Chan, European Radar Conference, EURAD, 2005 (unpublished), pp. 267–270.
- ⁶A. M. Tang, D. F. Kacher, E. Y. Lam, M. Brodsky, F. A. Jolesz, and E. S. Yang, *IEEE-EMBS*, 2603 (2007).
- ⁷S. G. Nekolla, *PET and MRI in Cardiac Imaging, in Cardiac CT, PET and MR* (Wiley-Blackwell, UK, 2006).
- ⁸G.S. Tzanakos, A.B. Abche, E. Micheli-Tzanakou, T. Stahl, W. Xiaoming, and T. Yudd, *IEEE-EMBS*, 2, 1443 (2000).
- ⁹H. O. Yaroslav, S. J. Hanson, and B. A. Pearlmutter, *Advanced Image Processing in Magnetic Resonance Imaging* (Taylor & Francis, London, 2005), Chap. 8, pp. 223–265.
- ¹⁰M. Nahrendorf, J. U. Streif, K.-H. Hiller, K. Hu, P. Nordbeck, O. Ritter, D. Sosnovik, L. Bauer, S. Neubauer, P. M. Jakob, G. Ertl, M. Spindler, and W. R. Bauer, *Am. J. Physiol. Heart Circ. Physiol.* **290**, H2516 (2006).
- ¹¹V. Ntziachristos, A. G. Yodh, M. Schnall, and B. Chance, *Proc. Natl. Acad. Sci. U.S.A.* **97**, 2767 (2000).
- ¹²R. Noeske, F. Seifert, K. H. Rhein, and H. Rinneberg, *Magn. Reson. Med.* **44**, 978 (2000).
- ¹³A. Jeremic and A. Nehorai, *IEMBS* **1**, 1006 (2004).
- ¹⁴G. M. Nijm, S. Swiryn, A. C. Larson, and A. V. Sahakian, *Comput. Cardiol.* **33**, 269 (2006).
- ¹⁵S. R. J. Axelsson, *IEEE Trans. Geosci. Remote Sens.* **41**, 2703 (2004).
- ¹⁶J. Sachs and P. Peyerl, Proceedings of the 16th IEEE Instrumentation and Measurement Technology Conference, IMTC/99, 1999 (unpublished), Vols. 24–26, pp. 1390–1395.
- ¹⁷The Visible Human Project, U.S. National Library of Medicine, 8600 Rockville Pike, Bethesda, MD 20894, http://www.nlm.nih.gov/research/visible/visible_human.html.
- ¹⁸J. Sachs and P. Peyerl, Proceedings of the Fourth International Conference on Electromagnetic Wave Interaction with Water and Moist Substances, 2001 (unpublished), pp. 165–72.
- ¹⁹J. Sachs, *M-sequence Radar Ground Penetrating Radar*, IEE Radar, Sonar, Navigation and Avionics Series No. 15, 2nd ed., edited by D. J. Daniels (The Institute of Electrical Engineers, UK, 2004), pp. 225–237.
- ²⁰R. L. Peterson, R. E. Ziemer, and D. E. Borth, *Introduction to Spread Spectrum Communications* (Prentice-Hall, Englewood Cliffs, NJ, 1995).
- ²¹Amtsblatt Nr. L 247 vom 21/09/2007/S. 0021-0055, <http://eur-lex.europa.eu/LexUriServ/LexUriServ.do?uri=OJ:L:2007:247:0021:01:DE:HTML>.
- ²²S. Gabriel, R. W. Lau, and C. Gabriel, *Phys. Med. Biol.* **41**, 2251 (1996).
- ²³R. E. Collin, *Field Theory of Guided Waves*, IEEE Press Series on Electromagnetic Wave Theory, 2nd ed. (IEEE, New York, 1991).
- ²⁴U. Schwarz, M. Helbig, J. Sachs, F. Seifert, R. Stephan, F. Thiel, and M. Hein, Proceedings of the 2008 IEEE International Conference on Ultra-Wideband (ICUWB) (IEEE, New York, 2008), Vol. 1, pp. 5–8.
- ²⁵W. J. Krzanowski, *Principles of Multivariate Analysis*, revised. ed. (Oxford University Press, New York, 2000).